Int. J. Multiphase Flow Vol. 17, No. 2, pp. 227–245, 1991
Printed in Great Britain.

0301-9322/91 $3.00 + 0.00

HYDRODYNAMIC MECHANISMS IN THE HORIZONTAL SLUG PATTERN

D. MOALEM MARON,[1] N. YACOUB,[1] N. BRAUNER[1] and D. NAOT[2]

[1]Department of Fluid Mechanics and Heat Transfer, Faculty of Engineering, University of Tel-Aviv, Ramat-Aviv 69395, Israel

[2]Center for Technological Education, Holon 58102, Israel

(Received 5 January 1990; in revised form 13 October 1990)

Abstract—The slug flow pattern is associated with an intensive mixing zone at its frontal region, where the fast-moving liquid slug front overruns the substrate film ahead. This mixing zone demonstrates intense fluctuations and asymmetry of the various flow characteristics, which clearly can not be treated analytically. An attempt to provide some insight into the complexity of the hydrodynamic mechanisms in the mixing zone is made by applying the k–l, k–ϵ models and numerically evaluating the various hydrodynamic characteristics. Particular boundary conditions at the free-moving interface have been developed and incorporated in the numerical simulation.

Key Words: horizontal, gas–liquid, slug, plug, mixing zone, turbulence models

1. INTRODUCTION

Two-phase gas–liquid slug flow is considered as an extremely complicated flow pattern. The complexity evolves from the intermittency of the flow and the large velocity gaps between the various slug regions. Consequently, slug flow incorporates a variety of hydrodynamic mechanisms and therefore no single solution strategy is expected to adequately encompass all slug regions. These difficulties have been tackled by resorting to a piecewise modelling approach, which utilizes the integral continuity and momentum equations, simplified according to the specific physical model assumed at each of the slug zones. For instance, separate models have been proposed for the liquid slug core, the slug tail (which ends at a relatively thin substrate film) and the adjacent elongated large bubble ahead of the fast-moving liquid slug front. Such mechanistic models provided reasonable predictions of the slug macrostructure and mean characteristics, mainly average cross-sectional velocities and pressure drop over a slug unit; e.g. to name but a few of these models: Kordyban & Ranov (1970), Dukler & Hubbard (1975), Nicholson *et al.* (1978) and Moalem Maron *et al.* (1982) for horizontal slug flow; and Bonnecaze *et al.* (1971), Fernandes *et al.* (1983), Orell & Rembrand (1986) and Sylvester (1987) for inclined or vertical slug flows.

It is to be emphasized here that integral approaches in slug modelling, though yielding acceptable results when compared with experimental data, are not capable of accounting for the detailed velocity distribution and of providing an insight into the associated complex instantaneous behaviour of the wall shear stress and other momentum transport phenomena. Understanding the fluctuating nature of the phenomena is of great interest, not only for improving the modelling of momentum and transport in slug flow, but also from other practical aspects, e.g. the relation between flow conditions and observed pipe damage (Kvernvold *et al.* 1984).

Among the various slug zones, the hydrodynamics of the frontal region probably are considered the most complicated. The fast slug front overruns the relatively slow substrate film ahead. The substrate fluid picked-up by the slug front is thus accelerated and mixes in within the front region. The mixing region extends well into the slug core region, where a fully-developed symmetric velocity distribution is established. Obviously, the frontal region demonstrates intense fluctuations and asymmetry of the flow characteristics, such as pressure gradients, wall shear etc. Note that the hydrodynamic patterns in the slug front region are expected to resemble those obtained in flows into sudden expansions (Bradshaw & Wang 1972). However, the phenomena associated with the moving slug front are of a higher degree of complexity due to the moving free interface.

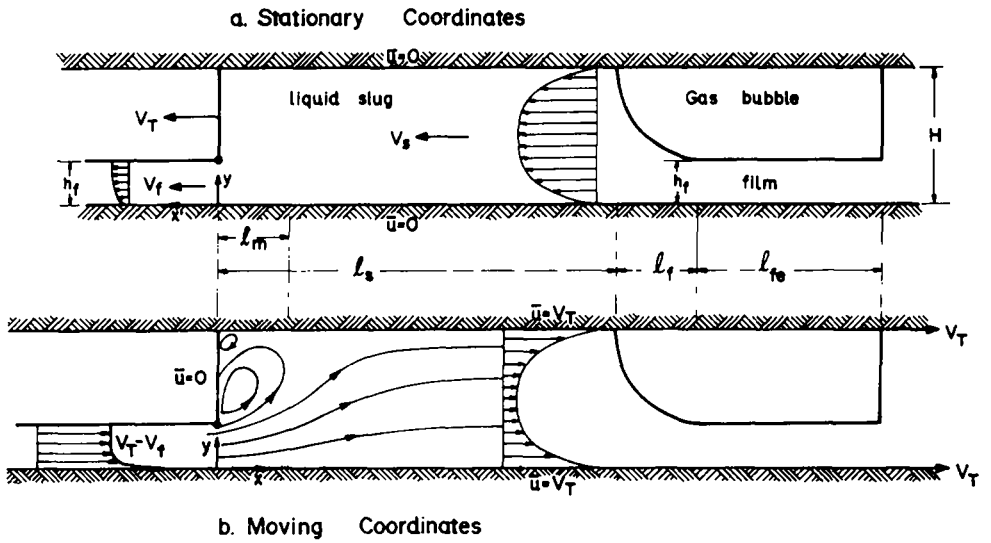

Figure 1. Schematic description of the physical model and coordinates systems.

In view of its hydrodynamic complexity, the front region has been treated in overall slug modelling by partial and unestablished approximations, mainly for estimating its length (Dukler & Hubbard 1975). Other basic characteristics, such as pressure drop or wall shear stress variation, require a thorough solution of the velocity field.

It is the main objective of the present work to explore via numerical simulations the flow field at the liquid slug front, in an attempt to provide some insight and understanding of the hydrodynamics in this rather complicated region.

2. THE PHYSICAL PICTURE

A schematic description of the physical phenomena associated with a typical horizontal slug unit is given in figure 1 in both stationary (a) and moving (b) coordinates systems. For simplicity, two-dimensional slug flow between parallel plates is considered. An idealized fully-developed flow is assumed, whereby a slug unit consists of a large lump of liquid which steadily travels over a thin smooth substrate film separating the liquid lumps. The liquid velocity in the liquid slug is several times greater than the mean velocity of the substrate film ahead, thus slow-moving material is continuously overrun by the fast-moving front of the slug and is accelerated to the fluid velocity in the liquid slug, forming a mixing eddy which penetrates a distance l_m into the slug front. Simultaneously with this pick-up process at the front, the slug sheds liquid from its back, forming a trailing decelerating film, to be picked-up by the successive slug front. Clearly, when the rate of liquid pick-up at the front equals the rate of liquid shedding at the rear, the length of the slug stabilizes (Dukler *et al.* 1985).

The idea of a mixing zone at the front accompanied by a shedding process at the back of the slug implies a recurrent momentum exchange in the slug. For instance, the boundary layers adjacent to the walls are periodically distorted in the mixing region at the front of the slug and are reestablished in the body of the slug behind the mixing region (Moalem Maron *et al.* 1982). A fully-developed velocity profile is obtained if the liquid slug is long enough.

Previous slug modelling refers mainly to the hydrodynamic picture in the slug core and slug trail. However, the complicated frontal mixing region has not been treated yet, and therefore demands special emphasis in the present work.

3. GOVERNING EQUATIONS AT THE SLUG FRONTAL REGION

The slug frontal region, where the slow substrate film ahead is overrun and accelerated, is hydrodynamically the more complicated zone and as such is hard to tackle analytically. The present treatment of the slug front region is based on a numerical simulation, which has been recently

developed by the authors studying the vortex region formed by a wall jet entering a free interface liquid bulk (Yacoub *et al.* 1991; Naot *et al.* 1989). The governing equations and *relevant* boundary conditions with reference to slug flow, as in figure 1(b) are:

$$-\Omega = \frac{\partial \bar{u}}{\partial y} - \frac{\partial \bar{v}}{\partial x} = \frac{\partial^2 \psi}{\partial x^2} + \frac{\partial^2 \psi}{\partial y^2} \qquad [1]$$

and

$$\bar{u}\frac{\partial \Omega}{\partial x} + \bar{v}\frac{\partial \Omega}{\partial y} = \frac{1}{\rho}\left[\left(\frac{\partial^2}{\partial x^2} - \frac{\partial^2}{\partial y^2}\right)\tau_{xy} + \frac{\partial^2}{\partial x\,\partial y}(\tau_{yy} - \tau_{xx})\right], \qquad [2]$$

where [1] represents the two-dimensional vorticity, Ω, in terms of a stream function, ψ, which satisfies the continuity equation, while [2] represents the vorticity transport equation. The stresses are modelled by an effective scalar viscosity, ν_e:

$$\frac{1}{\rho}\tau_{xy} = \nu_e\left(\frac{\partial \bar{u}}{\partial y} + \frac{\partial \bar{v}}{\partial x}\right), \quad \nu_e = \nu + \nu_t; \qquad [3a]$$

and

$$\frac{1}{\rho}(\tau_{yy} - \tau_{xx}) = 2\nu_e\left(\frac{\partial \bar{v}}{\partial y} - \frac{\partial \bar{u}}{\partial x}\right). \qquad [3b]$$

Hence, [2] becomes

$$\bar{u}\frac{\partial \Omega}{\partial x} + \bar{v}\frac{\partial \Omega}{\partial y} = \frac{1}{\nu_e}\left[\frac{\partial}{\partial x}\left(\nu_e^2\frac{\partial \Omega}{\partial x}\right) + \frac{\partial}{\partial y}\left(\nu_e^2\frac{\partial \Omega}{\partial y}\right)\right] + S_\Omega, \qquad [4a]$$

where

$$S_\Omega = -\left[4\frac{\partial^2 \nu_e}{\partial x\,\partial y}\frac{\partial^2 \psi}{\partial x\,\partial y} + \left(\frac{\partial^2 \nu_e}{\partial x^2} - \frac{\partial^2 \nu_e}{\partial y^2}\right)\left(\frac{\partial^2 \psi}{\partial x^2} - \frac{\partial^2 \psi}{\partial y^2}\right)\right]. \qquad [4b]$$

In this formulation the vorticity source, S_Ω, maintains symmetry between the role of the viscosity and the stream function, simplifying the accurate central difference discretization of this term. Moreover, in the particular form of [4a], the first derivatives of the viscosity, ν_e (which are large close to the wall), are avoided in [4b]. The non-linear use of the effective viscosity in the vorticity diffusion term increases the stability and accuracy of the discretization of this term. The effective viscosity, ν_e, in the above equations is related to the molecular viscosity, ν, and the turbulent eddy viscosity for high Reynolds number, ν_t. As the liquid slug flow is associated with high Reynolds numbers, two turbulence models, k–l and k–ϵ, aimed at synthesizing an "eddy viscosity" for evaluating the Reynolds stresses, have been used in parallel, in conjunction with [1 and 2]. The k–l model is represented by a partial differential equation for the turbulent energy, k:

$$\bar{u}\frac{\partial k}{\partial x} + \bar{v}\frac{\partial k}{\partial y} = \frac{\partial}{\partial x}\left(\frac{\nu_t}{\sigma_k}\frac{\partial k}{\partial x}\right) + \frac{\partial}{\partial y}\left(\frac{\nu_t}{\sigma_k}\frac{\partial k}{\partial y}\right) + \Pi - \epsilon, \qquad [5a]$$

where Π and ϵ are the turbulent energy production and turbulent energy dissipation, respectively;

$$\Pi = -\overline{u'v'}\left(\frac{\partial \bar{u}}{\partial y} + \frac{\partial \bar{v}}{\partial x}\right) - \overline{u'^2}\frac{\partial \bar{u}}{\partial x} - \overline{v'^2}\frac{\partial \bar{v}}{\partial y} \qquad [5b]$$

and

$$\epsilon = \frac{C_\mu^{3/4} k^{3/2}}{l}. \qquad [5c]$$

The eddy viscosity, ν_t, in terms of the turbulent energy and dissipation (mixing) length, l, is

$$\nu_t = C_\mu^{1/4} k^{1/2} l. \qquad [6]$$

In [5] and [6], σ_k and C_μ are constants.

The k–ϵ model includes an additional differential equation for the turbulent energy dissipation, ϵ:

$$\bar{u}\frac{\partial \epsilon}{\partial x}+\bar{v}\frac{\partial \epsilon}{\partial y}=\frac{\partial}{\partial x}\left(\frac{\nu_t}{\sigma_\epsilon}\frac{\partial \epsilon}{\partial x}\right)+\frac{\partial}{\partial y}\left(\frac{\nu_t}{\sigma_\epsilon}\frac{\partial \epsilon}{\partial y}\right)+C_{\epsilon 1}\frac{\epsilon}{k}\Pi-C_{\epsilon 2}\frac{\epsilon^2}{k}, \quad [7]$$

with

$$\nu_t=C_\mu\frac{k^2}{\epsilon}, \quad [8]$$

where σ_ϵ, $C_{\epsilon 1}$ and $C_{\epsilon 2}$ are empirical constants.

The possibility of deriving a transport equation for the dissipation length directly from the two model transport equations for k and ϵ has been used elsewhere (Yacoub *et al.* 1991; Naot *et al.* 1990). It was shown that for homogeneous turbulence in local equilibrium, $\Pi=\epsilon$, the transport equation for the length scale degenerates to a form that depends on the field geometry and boundary conditions only. The degenerated equation yields geometric scales that describe qualitatively the dissipation length scales obtained from calculations made with the full transport equation for the dissipation. For some simple cases of channel flow the agreement is remarkable. However, it has been shown (Naot *et al.* 1990) that in the present case the effects of the turbulence diffusion, convection and heterogeneity are too significant to be overlooked and the replacement of the transport equation for ϵ by a geometric specification of a length scale may affect the results substantially. The idea of using geometric specification for the scale was therefore abandoned as it was considered to be an oversimplification.

Equations [1] and [2] are to be solved simultaneously with [5] and [7] and the appropriate boundary conditions. These are:

$$y=0 \quad \bar{v}=0; \quad \bar{u}=V_T; \quad \psi=0; \quad [9a]$$

$$y=H \quad \bar{v}=0; \quad \bar{u}=V_T; \quad \psi=h_f(V_1-V_f)=\gamma; \quad [9b]$$

$$x\to\infty \quad \bar{v}=0; \quad \frac{\partial}{\partial x}(\bar{u},\bar{v},\psi,\Omega,k,\epsilon)\to 0; \quad [9c]$$

$$x=0 \quad 0\leqslant y\leqslant h_f \quad \bar{u}=f(y); \quad [9d]$$

and

$$x=0 \quad h_f<y<H \quad \bar{u}=0; \quad \frac{\partial k}{\partial x}=0; \quad \frac{\partial \epsilon}{\partial x}=0; \quad \psi=\gamma; \quad \Omega\simeq\frac{\partial \bar{v}}{\partial x}. \quad [9e]$$

Equations [9a, b] represent the no-slip conditions at the two bounding walls in the moving coordinates system. However, since [5] and [7] are not applicable at the walls, a logarithmic turbulent velocity profile is utilized in the near-wall regions over the first grid. Thus, at $y_1=\Delta y$ (see appendix A):

$$\bar{u}=V_T-v^*\left[2.5\ln\left(\frac{y_1 v^*}{\nu}\right)+5.0\right],$$

$$\psi_1=\int_0^{y_1}\bar{u}\,dy=v^* y_1\left[\frac{V_1}{v^*}-2.5\ln\left(\frac{y_1 v^*}{\nu}\right)-2.5\right]=\bar{u}y_1+2.5v^* y_1,$$

$$\Omega\simeq-\frac{\partial \bar{u}}{\partial y}=\frac{2.5v^*}{y_1},$$

$$k=\frac{v^{*2}}{\sqrt{C_\mu}}=3.3v^{*2},$$

$$\epsilon=\frac{2.5C_\mu^{3.4}k^{3.2}}{y_1}, \quad [10]$$

where v^* is the local shear velocity. Similar treatment is made near the upper wall over the last grid at point $y = H - \Delta y$, as detailed in appendix A. Equation [9c] implies that for sufficiently long slugs, fully-developed conditions are obtained.

The most complicated boundary is at $x = 0$, which is divided into three regions:

(a) For $y < h_f$, the entry conditions are due to the entering substrate film, whereby for a turbulent film condition [9d] becomes:

$$\bar{u} = V_T - v^*\left[2.5 \ln\left(\frac{yv^*}{\nu}\right) + 5.0\right]; \quad \bar{v} = 0;$$

$$\Omega = -\frac{\partial \bar{u}}{\partial y} = \frac{2.5v^*}{y}; \quad k = 3.3v^{*2}\left(1 - \frac{y}{h_f}\right);$$

$$\psi = \int_0^y \bar{u}\, dy = \bar{u}y + 2.5v^*y;$$

$$l = 0.4y; \quad \epsilon = \frac{C_\mu^{3/4} k^{3/2}}{l}. \qquad [11a]$$

Note that, k is assumed to decay linearly from its wall value to zero at the free surface. However, it is to be noted that values of k and ϵ in this region are very small and their contribution is practically negligible. For a laminar substrate film condition [9d] reads:

$$\bar{u} = V_T - \frac{2V_f y}{h_f}; \quad \bar{v} = 0;$$

$$\Omega = \frac{2V_f}{h_f}; \quad k = 0, \epsilon = 0;$$

$$\psi = V_T y - \frac{V_f y^2}{h_f}. \qquad [11b]$$

(b) For $y > h_f$, the gas–liquid interface represents the slug front line where the velocity is V_T (or zero in moving coordinates). As the gas–liquid interface at the slug frontal region is vertical, it was necessary to revise the boundary condition for the dissipation, formulated for open channel flow (Hossain & Rodi 1980), and adjust it for a vertical surface [Naot *et al.* (1989); see appendix B]. Indeed, as was expected, the numerical tests showed local augmentation of the dissipation close to the interface. However, as the region influenced is almost stagnant (in the moving coordinates system), the overall effect on the velocity distribution is negligible and the use of the simple conditions [9e], based on the premise that turbulent energy or dissipation do not cross the free interface, at $x = 0, h_f < y < H$, was practically confirmed.

(c) At $x = 0$, $y = h_f$, the substrate thin film meets the liquid slug and a shear layer is developed due to the abrupt drop in velocity. This is translated into a vorticity source, by averaging $(\bar{u}\Omega)$ at point $(x = 0; y = h_f)$ along a grid height Δy, which includes this point. Since the dominant contribution to the vorticity at the "velocity discontinuity region" is due to the singular behaviour of $(\partial \bar{u}/\partial y)$, the vorticity convected into the adjacent cell, represented in the numerical procedures as a vorticity flux corresponding to a vorticity ω_0, becomes:

$$\int_{h_f - \frac{\Delta y}{2}}^{h_f + \frac{\Delta y}{2}} \bar{u}\Omega\, dy = \frac{u_0^2 f_0}{2} = u_0 \omega_0 \Delta y, \qquad [12]$$

where, u_0 is the velocity at the upper layer of the penetrating substrate and f_0 is of the order of unity. The representative vorticity, ω_0, is thus

$$\omega_0 = \frac{f_0 u_0}{(2\Delta y)}, \qquad [13]$$

which is used as a boundary condition at the point ($x = 0$; $y = h_f$). The sensitivity of the streamline configuration to the specific choice of f_0 has been studied elsewhere (Yacoub *et al.* 1991). Numerical tests show that streamline contraction occurs at the impingement point of the film into the slug for $f_0 > 1$, whereas with $f_0 < 1$, streamline divergence is observed. In the present work horizontal streamlines at this point are assumed, and $f_0 \approx 1$ has been used.

The numerical calculation has been performed with a 20×80 grid, with 20 nodes evenly distributed in the vertical direction and 80 nodes distributed with variable spacing in the horizontal direction (Yacoub 1989). Central point discretization was employed for all the derivatives apart from the convective derivatives, for which the upwind technique was used. Using values for some variables taken from the former iteration, the linearized equations in the finite difference formulation were organized in a mode amenable to the alternating direction implicit integration (ADI) algorithm. The grid was swept solving for a whole line or a whole column at each step with a tri-diagonal matrix (TDM) solver. Each iteration consists of four grid sweeps vertically, horizontally, backwards and forwards (not necessarily in this order).

To avoid divergence at an early stage in the calculations, the updating of the variables at each iteration was relaxed during the first 50 iterations. Convergence was monitored by calculating the errors in satisfying the discretized equations for ψ and Ω. Reduction of the relative errors to 10^{-5} was established within 150 iterations, or 500 grid sweeps consuming 400 (CPU) s on a CDC 6600 computer.

Experiments with a fine 40×80 grid indicated small ($< 1\%$) grid effects due to the dependency of [13] for ω_0 on Δy, and due to the differences between Δy and Δx in the main flow field. Close to the wall, theoretical expressions exist for the dependencies of Ω, ϵ and v_t on the distance from the wall. These have been utilized to estimate the discretization errors close to the walls. Indeed, the numerical experiments showed small grid effects close to the wall, which may be considered as an indication for the entire field. For more details, the reader is referred to the description of the numerical method in Yacoub *et al.* (1991).

4. CALCULATED RESULTS AND DISCUSSION FOR THE SLUG MIXING ZONE

The initiation of the numerical simulation requires the geometrical parameters H, h_f, the slug translational velocity, V_T, and the entering flux, γ. As detailed in appendix C, the entering mass flux is identified with the slug pick-up rate γ, and is obtained with V_T and h_f (and other slugs parameters) for a given set of liquid and gas superficial velocities, U_{LS} and U_{GS}, and slug frequency, f. Clearly, the numerical scheme can be initiated for any given physical situation (defined by the geometry and flow rate parameters) of a free wall jet entering into a liquid lump. Here, however, the results are presented in relation to an unaerated slug flow pattern (obtained for specified U_{GS}, U_{LS}, f and $R_S = 1$) and by assuming zero drift velocity in the model for V_T ($V_d = 0$ in [C.8]). The effect of the drift velocity will be discussed separately (figure 12).

Figures 2 and 3 show typical $\bar{u}$, $\bar{v}$ and ψ contours along the liquid slug zones for $H = 1$ cm, and various combinations of U_{LS}, U_{GS} and f [within the observed range for the slug flow pattern (Dukler & Hubbard 1975)]. Also included in figure 2(c) are the specific lines of $\bar{u} = 0$ and $\bar{v} = 0$, the intersection of which defines stagnation points (in the moving coordinates system). Inspection of figures 2 and 3 indicates that four stagnation points can be identified; the first is S_1, located at the vertical free interface $x = 0$, $y > h_f$, where $\bar{u} = 0$. Above and below point S_1, the $\bar{v}$ components are in opposite directions, both degenerate at S_1. The second stagnation point S_2, is situated at the saddle-point formed between the large vortex (moving backwards) and the small upper wall vortex (moving forwards). The other two stagnation points S_3 and S_4 correspond to the center points of the two vortices. The streamlines at $x = 0$ first circulate backwards around the large vortex and then at some location reverse forwards to the main flow direction. A streamline exists for which the flow is just forward, with an inflection point. Below this streamline and far enough downstream of the entry of the wall jet, fully-developed $\bar{u}$, $\bar{v}$ and ψ lines are obtained.

The approach towards a developed flow distribution downstream of the liquid slug (upstream in stationary coordinates), with simultaneous stabilization of other related hydrodynamic variables is further demonstrated in figures 4–6. In figure 4, the calculated wall shear stresses for the upper

and lower boundaries are compared. At $x = 0$, where the liquid film meets the liquid slug, the lower wall shear stress starts increasing from its film value to an equilibrium level, whereas the upper wall shear first decreases very rapidly to a minimum and then increases again before it decreases to its equilibrium level. The extremum points depend on the location and size of the small and large vortices. The equilibrium levels of both the lower and upper shear stresses correspond to the wall shear of fully-developed flow with a flow rate of $(V_T - V_s)H$. Included in figure 4 is a curve-fit of $x^{-0.2}$, based on the developing boundary layer wall shear stress obtained on a continuous moving surface in a turbulent regime (Sakiadis 1961). As is shown in figure 4, a better fit is obtained for the higher velocities where the flow is fully turbulent. This implies that the use of a boundary layer model in slug modelling may be reasonable (Moalem Maron *et al.* 1982; Dukler *et al.* 1985).

One of the main characteristics of slug flow is the (periodic) variation in the pressure drop. An overall momentum balance between the entry at $x = 0$ and an x location within the liquid slug reads

$$P_x - P_0 = \frac{1}{H}\left[\int_0^x (\tau_{wt} + \tau_{wb})\,dx + \int_0^{h_f} \rho \bar{u}_f^2\,dy - \int_0^H \rho \bar{u}_x^2\,dy - \int_0^{h_f} \rho g(h_f - y)\,dy - \int_0^H \rho g(H - y)\,dy\right], \quad [14]$$

whereby

$$\Delta P_s = P_x - P_0 = \Delta P_f + \Delta P_a + \Delta P_h. \quad [15]$$

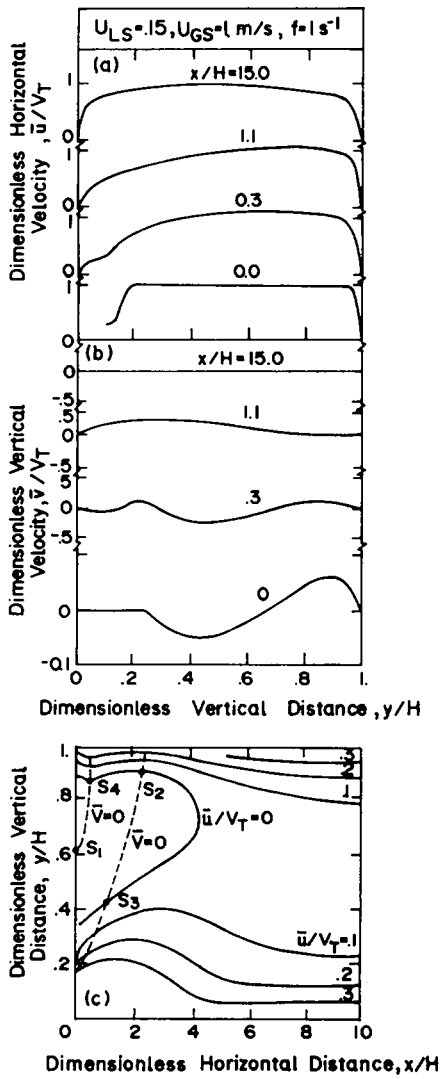

Figure 2. Axial and normal velocity profiles and contours.

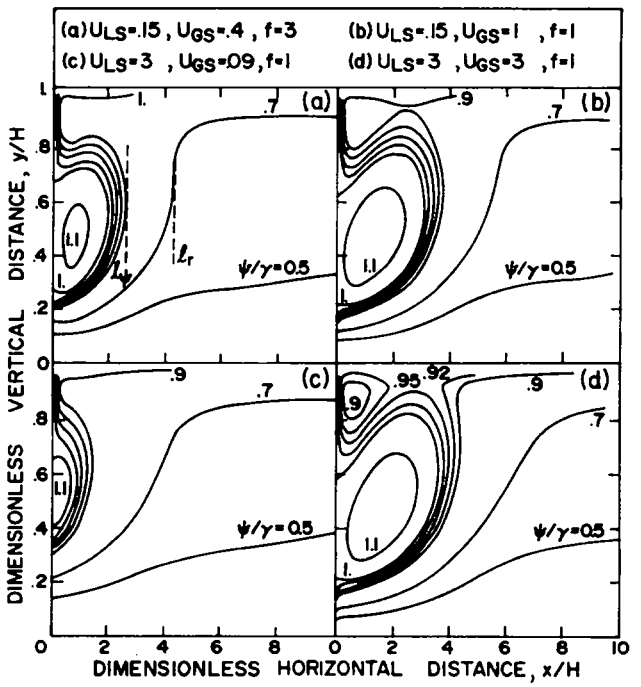

Figure 3. Streamlines in the moving coordinates system for various operational conditions.

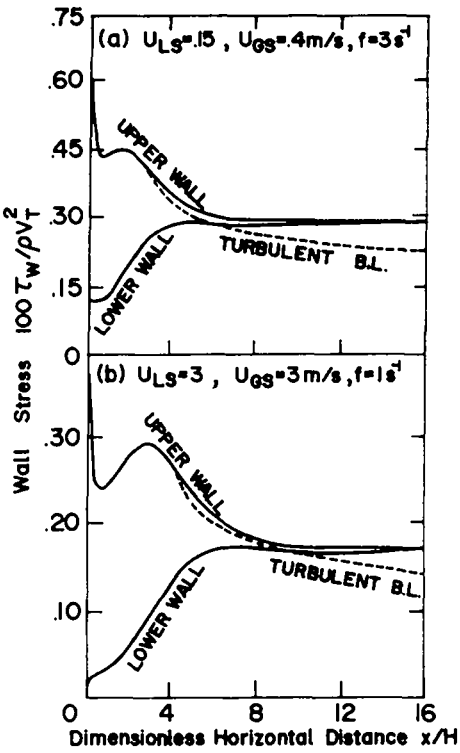

Figure 4. Wall shear stresses at the upper and lower walls.

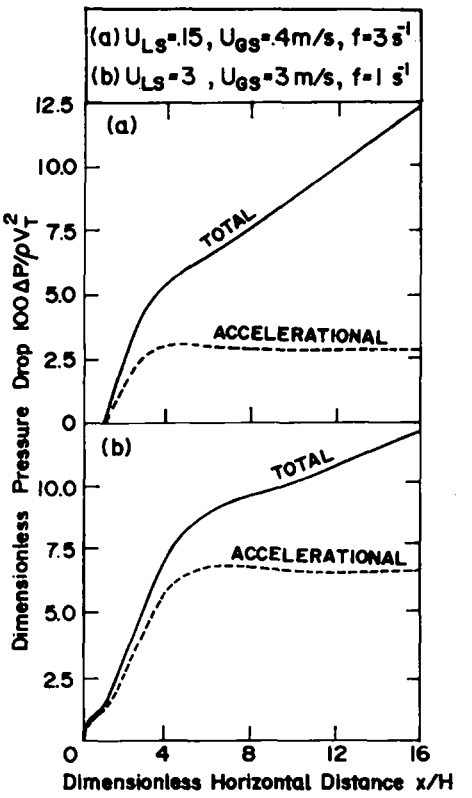

Figure 5. Accelerational and total pressure drop along the liquid slug core.

Thus, [14] and [15] indicate that the total pressure variation in the liquid slug is composed of three components due to friction, acceleration and hydrostatic head, ΔP_f, ΔP_a, and ΔP_h, respectively. The latter, is found to be practically negligible here (H = 1 to 2 cm), compared with the frictional and acceleration contributions. As is demonstrated in figure 5, in the well-developed region the acceleration term becomes constant, while the frictional term maintains the expected constant slope. It is to be noted that a negative acceleration pressure drop may result [as in figure 5(a)] at the slug entry region where the substrate film enters the slug core. This indicates that initially the entering substrate jet (in moving coordinates) accelerates due to local contraction [see figure 3(a)]. Similar contraction and acceleration effects are well-known in jet flow through sudden expansions.

Figure 6 represents the dissipation rate calculated in two ways. The first method is direct integration of the local dissipation, ϵ, as evaluated along the numerical procedure

$$E_d = \int_0^x \int_0^H \epsilon \, dy \, dx. \qquad [16]$$

The second method is based on applying an energy balance, whereby the total dissipation, from the entry to any downstream location x, is obtained by integration of the wall shear, while considering the gain in pressure and kinetic energy. Thus,

$$E_d = V_T \int_0^x (\tau_{wt} + \tau_{wb}) \, dx - \gamma(P_x - P_0) - \tfrac{1}{2}\rho\left(\int_0^H \bar{u}_x^3 \, dy - \int_0^{h_f} \bar{u}_f^3 \, dy\right). \qquad [17]$$

Substituting [14] for the pressure term and [C.1] for γ in [17] yields:

$$E_d = V_s \int_0^x (\tau_{wt} + \tau_{wb}) \, dx - \rho V_s\left(\int_0^{h_f} u_f^2 \, dy - \int_0^H \bar{u}_x^2 \, dy\right) + \frac{\rho}{2}\left(\int_0^{h_f} u_f^3 \, dy - \int_0^H \bar{u}_x^3 \, dy\right). \qquad [18]$$

As is demonstrated in figure 6, the agreement between [16], which represents a direct integration of the dissipation rate and [18], which is based mainly on velocity profiles in the near-wall regions reinforces the validity of the whole numerical simulation, including the use of the k–ϵ model.

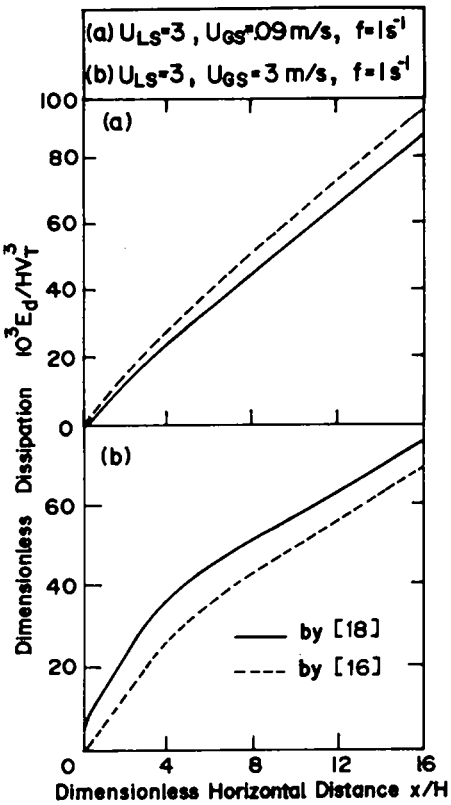

Figure 6. Energy dissipation rate along the liquid slug core.

Note again, that the region where the slope of the dissipation rate remains constant represents fully-developed conditions. However, with weak vortices [figure 6(a) which corresponds to figure 3(c)], the change in the dissipation rate across the mixing zone is moderate, while for strong vortices [figure 6(b) which corresponds to figure 3(d)] a sharp rise in the dissipation rate in the mixing zone is demonstrated. The contours of equal vorticity lines and the turbulent structure in terms of equi-turbulent energy lines and equi-dissipation length lines are detailed elsewhere (Yacoub *et al.* 1991).

As stated earlier, the main objective of the present paper is to derive some insight and characterization of the frontal region. For instance, one can identify the core of the front region by the location of the large vortex centre, which is one of the four stagnation points located in this region. Figure 7 includes the dimensionless horizontal and vertical coordinates (x_c, y_c) of the large vortex centre as functions of the input slug parameters. Clearly, large x_c implies a larger vortex, hence an extended mixing zone. The non-dimensional vertical position of the vortex centre is practically constant, $y_c/H = 0.5$ (see also table 1).

The characterization of the mixing zone length is of particular interest in slug modelling. In view of the physical picture described above (as in figures 2–6), the following three characteristic lengths for the slug front region may be defined [see figure 3(a)]:

(a) The length l_ψ, defined by the location of the external closed streamline which originates at the discontinuity point, and envelopes the large vortex. This streamline separates the liquid which circulates within the eddy from that which continues forwards in the main flow direction, and therefore corresponds to $\psi = \gamma = h_f(V_T - V_f)$.

(b) The length, l_r, beyond which no flow reversal takes place. The streamline which defines l_r is the one demonstrating an inflection point (at $x = l_r$), beyond which the axial velocity components are always directed into the liquid slug core.

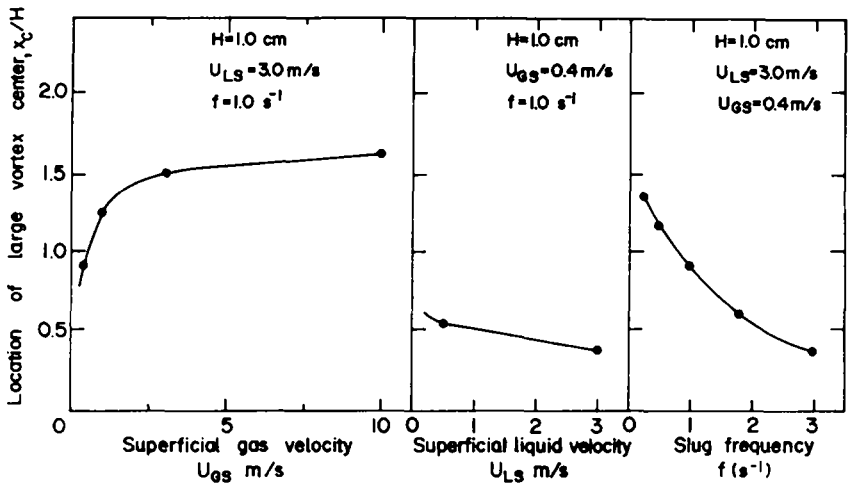

Figure 7. Location of a large vortex centre for various operational conditions.

(c) The distance, l_d, is related to the developing flow region and is defined here as the distance where the dissipation rate differs by less than, say 5% (a rather arbitrary criterion) from its ultimate level at fully-developed (one-dimensional) flow.

Figures 8–10 summarize the above characteristic length variation with the basic input slug parameters, U_{GS}, U_{LS} and f. As expected, the length of the circulating zone, l_ψ, is smaller than that of the reversed flow region, l_r, both of which are smaller than the required distance for establishing fully-developed flow (note that l_r crosses l_d in figure 9, implying that the arbitrary 5% criterion used to obtain l_d does not really ensure the establishment of fully-developed flow). Included in figures 8–10, is the empirical correlation suggested by Dukler & Hubbard (1975) for the length of the mixing zone, l_c, as used in previous studies. As is shown in the figures, this correlation poorly represents the length of the frontal region and its variation with the various slug parameters.

Inspection of figures 8–10 indicates that, in general, the effects of U_{LS} and U_{GS} on l_ψ, l_r or l_d are moderate, except for the low range of U_{GS}. A rather more pronounced effect is shown in figure 10 with the slug frequency. It is to be recalled at this point that the characteristics of circulation zones formed by entering jets are known to be determined mainly by the jet geometry and entering flow rate, both of which are identified in the case of slug flow with the relative substrate thickness, R_f, and the slug Reynolds number, $\mathrm{Re}_s = DV_s/\nu_L$. Therefore, the calculated R_f, as obtained based on U_{GS}, U_{LS} and f, are included in figures 8–10 for further interpretation. Indeed, figures 8–10 point out a consistent trend, whereby the mixing zone expands with decreasing R_f, which embodies the effects of U_{GS}, U_{LS} and f through the slug model governing equations (appendix C). The role of R_f is summarized in figure 11, showing that the length of the mixing zone is mainly correlated by the R_f and it decreases with increasing R_f.

Figures 2–11 relate to a given geometry $H = 1$ cm (or $D_h = 2$ cm). The effects of scale-up to larger conduits are demonstrated in table 1, with reference to $H = 2$ cm (or $D_h = 4$ cm). Obviously,

Table 1. Typical slug characteristics

H (cm)	R_f	V_T (m/s)	$V_T - V_s$ (m/s)	$V_T - V_f$ (m/s)	$\frac{l_\psi}{H}$	$\frac{l_r}{H}$	$\frac{l_d}{H}$	$\frac{x_c}{H}$	$\frac{y_c}{H}$
			$U_{LS} = 1.0 m/s$,	$U_{GS} = 1.0 m/s$,	$f = 1.0 s^{-1}$				
1.0	0.160	2.29	0.29	1.79	3.4	4.56	4.30	1.18	0.44
2.0	0.190	2.29	0.29	1.51	2.91	4.09	4.48	1.03	0.47
			$U_{LS} = 3.0 m/s$,	$U_{GS} = 1.0 m/s$,	$f = 1.0 s^{-1}$				
1.0	0.164	4.57	0.57	3.48	3.58	4.53	4.48	1.24	0.46
2.0	0.190	4.57	0.57	3.0	3.14	4.01	4.32	1.05	0.47
			$U_{LS} = 3.0 m/s$,	$U_{GS} = 3.0 m/s$,	$f = 1.0 s^{-1}$				
1.0	0.149	6.86	0.86	5.76	3.75	4.7	4.85	1.49	0.46
2.0	0.160	6.86	0.86	5.38	4.16	4.81	4.57	1.48	0.47

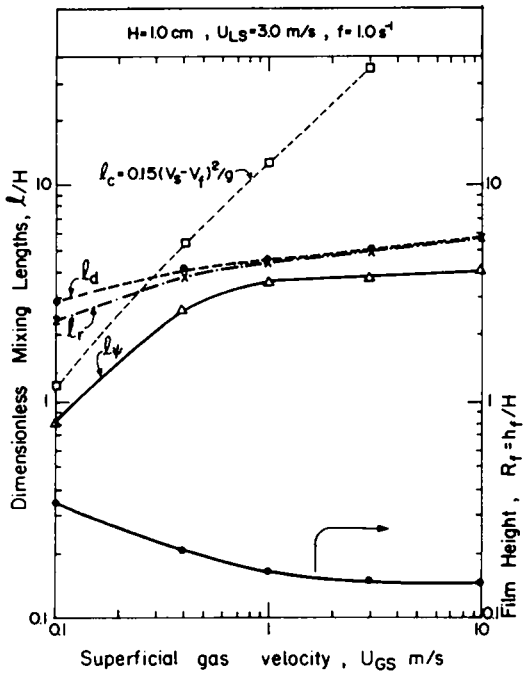

Figure 8. Mixing zone length as a function of the gas superficial velocity.

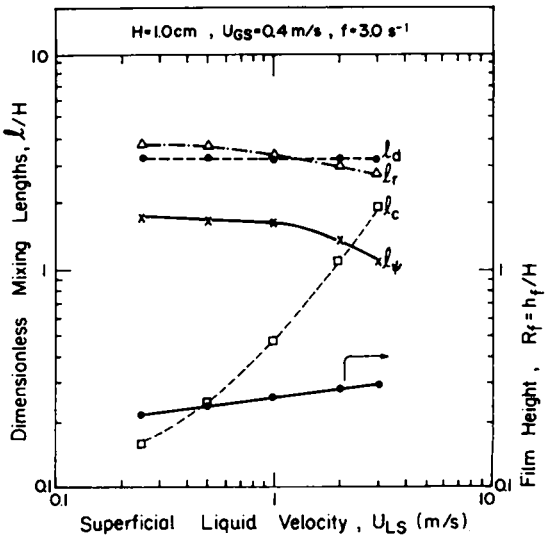

Figure 9. Mixing zone length as a function of the liquid superficial velocity.

increasing the geometrical dimensions requires significantly larger computational grids and therefore the results in table 1 are only aimed at identifying the typical trends of the mixing zone characteristics in scaling-up to larger conduits. In principle, increasing H, increases both Re_s and R_f. However, the resulting overall effect of H is rather mild. Consequently, the various non-dimensional characteristic lengths can be considered practically unaffected by the conduit size.

The results presented so far assume zero drift velocity, where for $n = 7$ in [C.8], $V_T/V_s = 8/7$. Figure 12 shows the effects of including a drift velocity, V_d, in modelling the slug translational velocity, as described in appendix C. For $D_h = 2$ in [C.9], $V_d = 0.24$ m/s which affects an increase of 2–20% in the V_T range studied here. In general, for identical U_{LS}, U_{GS} and f the inclusion of the drift velocity results in increased pick-up rate and substrate film thickness, R_f, as implied by [C.1]. Therefore as R_f increases, the mixing zone lengths l_ψ and l_r decrease (as expected in view of figure 11), and are similarly well-correlated by the corresponding R_f as shown in figure 12(b).

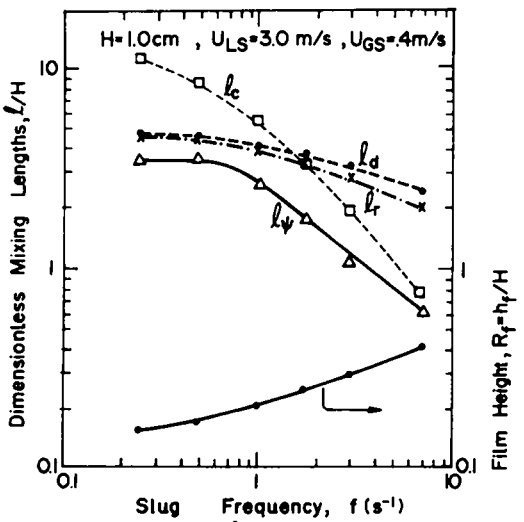

Figure 10. Mixing zone length as a function of the slug frequency.

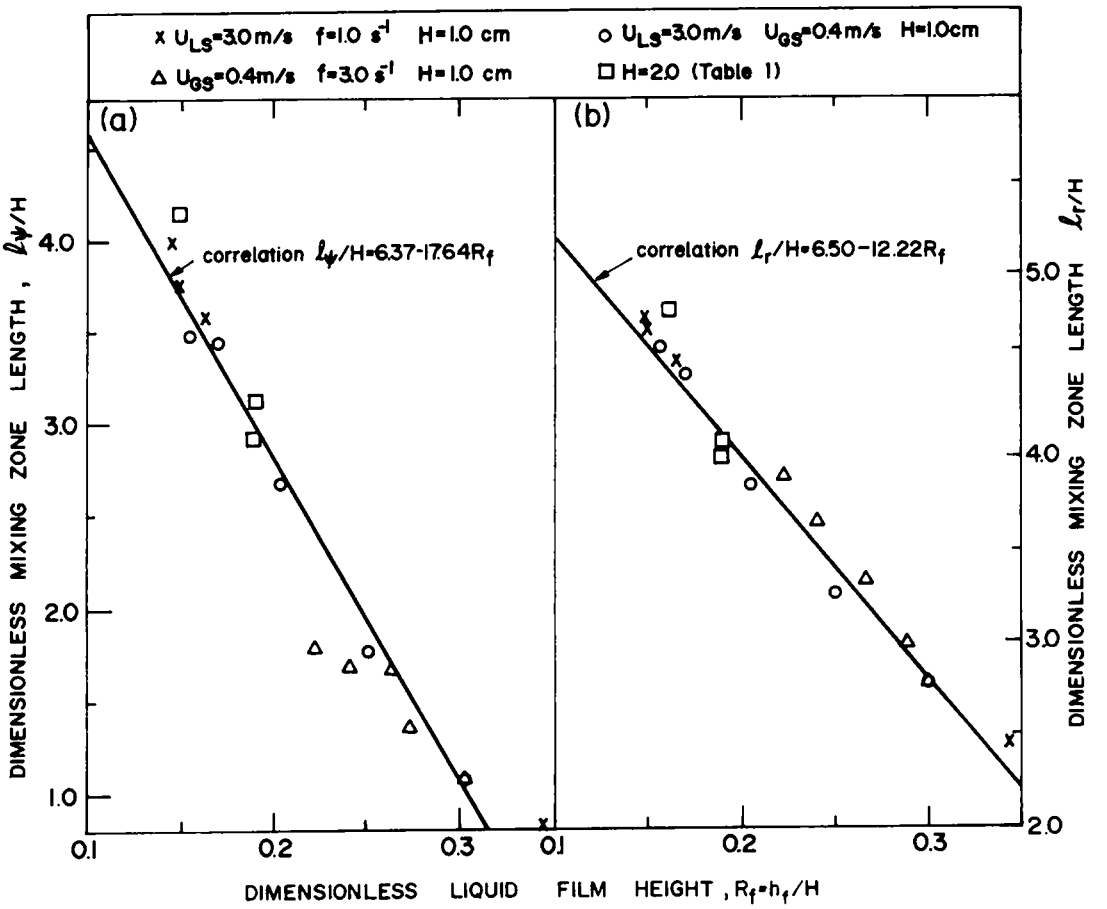

Figure 11. Mixing zone length as a function of the film thickness ahead.

However, for identical R_f, comparison of figures 11 and 12(b) indicates that higher l_ψ or l_r are obtained for a non-zero drift velocity.

On the other hand, l_d increases for a non-zero drift velocity since the centre velocity in the developed region (in moving coordinates) in this case asymptotically approaches a finite level, V_d (but not zero as with zero drift).

Note that the inclusion of drift velocity is in a sense equivalent to changing the V_T/V_s slope in [C.8] due to utilizing a different velocity profile in the slug core. Thus, the trends expected with different V_T/V_s can be deduced from the above-mentioned effects of a non-zero drift.

5. APPLICATION TO SLUG FLOW MODELLING

As described in appendix C, the complete set of governing equations for slug flow have been derived, based on continuity equations in stationary and moving coordinates systems, together with the momentum equations for the various slug zones. As noted earlier, previous studies on slug modelling utilized an *ad hoc* unestablished model for the mixing zone length, and referred only to accelerational pressure losses in this region.

Figure 13 shows typical variations of the frictional pressure losses in the slug front region relative to the ultimate level of the pressure drop in the well-developed slug core. The general trends in the entry region of the substrate film into the liquid slug resemble those obtained for sudden expansions (Bradshaw and Wang 1972) and are understandable in view of the circulation patterns shown in figure 3. The local frictional pressure gradient initially decreases due to the steep decrease in the upper wall shear stress very close to the entry plane at $x = 0$ (figure 4), then it recovers due to the cumulative shear stress built-up on the upper and lower walls. Finally, it drops back toward

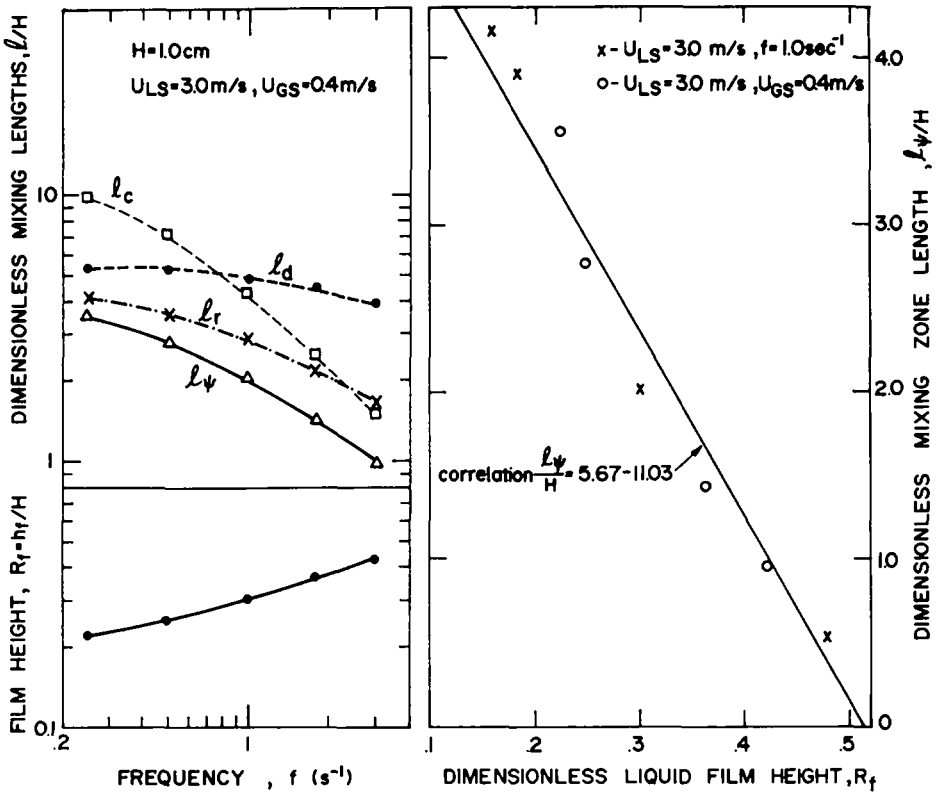

Figure 12. Effects of slug parameters on the mixing zone length with non-zero drift velocity.

its equilibrium level, whereupon the entry effect diminishes. Integrations of various plots, such as those shown in figure 13, indicate that the average frictional pressure drop in the mixing zone differs by $< 5\%$ from its asymptotic value far downstream. Thus, the contribution of the mixing zone to the friction pressure losses can be estimated reasonably by

$$(\Delta P_f)_{\text{mixing}} = \int_0^{l_m} \left(\frac{\partial p}{\partial x}\right)_f \mathrm{d}x \simeq l_m \left(\frac{\mathrm{d}p}{\mathrm{d}x}\right)_{f_{x\to\infty}}, \qquad [19]$$

where l_m stands for the various definitions of the mixing region length, as discussed with reference to figures 8–12. It is of interest to add that the inclusion of a drift velocity according to [C.9] does not alter the validity of [19]. Thus, [19] may be regarded as a rather general approximation which bears practical importance.

6. CONCLUDING REMARKS

The front of the slug core demonstrates circulating patterns (in moving coordinates) and intense local fluctuations and asymmetry of the hydrodynamic characteristics. Thus, the mixing zone is evidently of significance in predicting the overall transport rates in the slug flow pattern. The mixing zone length has been found mainly to be a function of the substrate film thickness. The wall shear at the upper surface is consistently higher than that of the lower tube surface and resembles that of a developing turbulent boundary layer.

The average frictional pressure drop in the mixing zone has been found to be practically equal to the well-developed frictional loss. Based on this result, its overall contribution to the total pressure drop can be conveniently included in slug modelling. The numerical simulation for the flow within the liquid slug core provides some sight into the various hydrodynamic characteristics, velocity contours, streamlines, stagnation points, vorticity, wall shear, pressure drop terms and turbulent energy and dissipation.

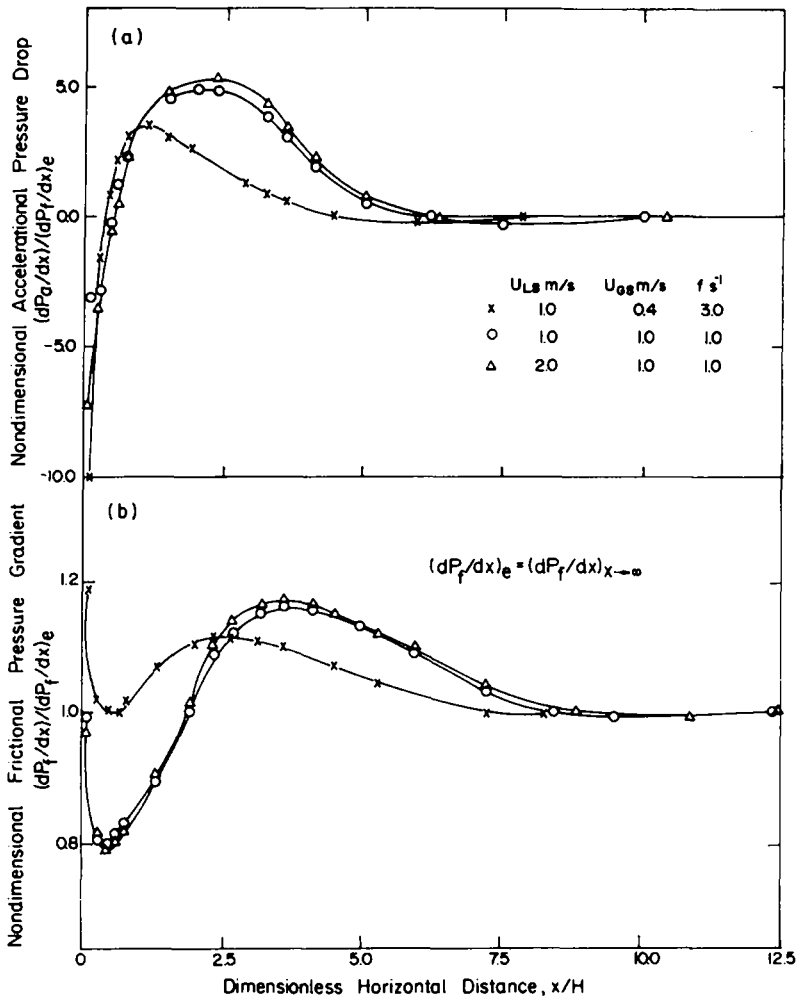

Figure 13. Frictional and accelerational pressure drops along the liquid slug.

REFERENCES

BARNEA, D. & BRAUNER, N. 1985 Holdup of the liquid slug in two phase intermittent flow. *Int. J. Multiphase Flow* **11**, 43–49.

BENDIKSEN, K. H. 1984 An experimental investigation of the motion of long bubbles in inclined tubes. *Int. J. Multiphase Flow* **10**, 467–483.

BENJAMIN, T. B. 1968 Gravity currents and related phenomena. *J. Fluid Mech.* **31**, 209–248.

BONNECAZE, R. H., ERISKINE, W. JR & GRESKOVICH, E. J. 1971 Holdup and pressure drop for two-phase slug flow in inclined pipes. *AIChE Jl* **17**(5), 1109–1113.

BRADSHAW, P. & WANG, F. Y. F. 1972 The reattachment and relaxation of a turbulent shear layer. *J. Fluid Mech.* **52**, 113–135.

DUKLER, A. E. & HUBBARD, M. G. 1975 A model for gas–liquid slug flow in horizontal and near horizontal tubes. *Ind. Engng Chem. Fundam.* **14**, 337–347.

DUKLER, A. E., MOALEM MARON, D. & BRAUNER, N. 1985 A physical model for predicting the minimum stable slug length. *Chem. Engng Sci.* **40**, 1379–1385.

FERNANDES, R. C., SEMIAT, R. & DUKLER, A. E. 1983 Hydrodynamic model for gas–liquid slug flow in vertical tubes. *AIChE Jl* **29**, 981–989.

HOSSAIN, M. S. & RODI, W. 1980 Mathematical modelling of vertical mixing in stratified channel flow. Presented at the *2nd Symp. on Stratified Flows*, Trondheim, Norway.

KORDYBAN, E. S. & RANOV, T. 1970 A flow model for two-phase slug flow in horizontal tubes. *J. bas. Engng* **92**, 857–864.

KVERNVOLD, O., VINDOY, V., SONTVEDT, T., SAASEN, A. & SELMER-OLSEN, S. 1984 Velocity distribution in horizontal slug flow. *Int. J. Multiphase Flow* **10,** 441–457.

MOALEM MARON, D., YACOUB, N. & BRAUNER, N. 1982 New concepts on the gas–liquid slug flow pattern. *Int. Commun. Heat Mass Transfer* **9,** 333–342.

NAOT, D., YACOUB, N. & MOALEM MARON, D. 1989 Open surface renewal boundary conditions for the k–ϵ turbulence model. In *Proc. 23rd IAHR—Int. Assoc. Hydraulic Research—Conf.*, Ottawa, Canada, Vol. A, pp. 293–299.

NAOT, D., YACOUB, N. & MOALEM MARON, D. 1990 Dissipation length scale dynamics. Presented at *The Beer Sheva Semin. on MDH-flows and Turbulence*, Beer Sheva, Israel.

NICHOLSON, M. K., AZIZ, K. & GREGORY, G. A. 1978 Intermittent two phase flow in horizontal pipes: predictive models. *Can. J. chem. Engng* **56,** 653–663.

ORELL, A. & REMBRAND, R. 1986 A model for gas–liquid slug flow for vertical tube. *Ind. Engng Chem. Fundam.* **25,** 196–206.

SAKIADIS, B. C. 1961 Boundary-layer behavior on continuous solid surfaces: II. The boundary layer on continuous flat surface. *AIChE Jl* **7**(2), 221–225.

SYLVESTER, N. D. 1987 A mechanistic model for two-phase vertical slug flow in pipes. *Trans. ASME J. Energy Resour. Technol.* **109,** 206–213.

UEDA, H., MOLLER, R., KOMORI, S. & MIZUSHINA, T. 1977 Eddy diffusivity near the free surface of open channel flow. *Int. J. Heat Mass Transfer* **20,** 1127–1136.

YACOUB, N. 1989 Hydrodynamic analysis of the frontal regions in periodic flows. Ph.D. Thesis, School of Engineering, Tel Aviv Univ., Israel.

YACOUB, N., NAOT, D. & MOALEM MARON, D. 1991 Numerical simulation of a horizontal slug front. *Int. J. numer. Meth. Fluids.* Submitted.

APPENDIX A

Thin Shear Layer Boundary Conditions

Close to the two plates, the numerical solution is matched with an analytic specification of the thin shear layer characterized by the logarithmic velocity profile and local equilibrium turbulence. The velocity profile is assumed to be logarithmic in the physical (stationary) coordinates system:

$$\bar{u} = V_T - v_p^* 2.5\left[\ln\left(\frac{v_p^* \eta}{\nu}\right) + 2\right], \qquad [A.1]$$

where $v_p^* = v_b^*$ and $\eta = y$ for the bottom plate, and $v_p^* = v_t^*$ and $\eta = H - y$ for the top plate. By integration, the stream functions adjacent to the bottom and top plates become:

$$\psi_b = \int_0^y \bar{u}\, d\eta = y\left\{V_T - 2.5 v_b^*\left[\ln\left(\frac{v_b^* y}{\nu}\right) + 1\right]\right\} \qquad [A.2a]$$

and

$$\psi_t = \gamma - \int_0^{H-y} \bar{u}\, d\eta = \gamma - (H-y)\left\{V_T - 2.5 v_t^*\left[\ln\left(\frac{v_t^*(H-y)}{\nu}\right) + 1\right]\right\}. \qquad [A.2b]$$

In the thin shear layer the $\bar{v}$ component vanishes and the vorticity depends on $d\bar{u}/dy$ only, thereby

$$\Omega_b = \frac{2.5 v_b^*}{y}, \qquad \text{bottom surface,} \qquad [A.3a]$$

and

$$\Omega_t = \frac{-2.5 v_t^*}{(H-y)}, \qquad \text{top surface.} \qquad [A.3b]$$

The specification of v_p^* determines the stream function and the velocity within the thin shear layers.

The thin shear layer is also characterized by the degeneration of the turbulence energy production $\Pi (= -\overline{u_i' u_j'}\, \partial \bar{u}_i / \partial x_j)$ to

$$\Pi = -\overline{u'v'}\frac{d\bar{u}}{dy}. \qquad [A.4]$$

Assuming the total shear stress $\tau_{tot} = \rho(-\overline{u'v'} + \nu\, d\bar{u}/dy)$ to be locally independent of the distance from the wall, and equal to the local shear stress ρv^{*2}, we note that in view of [A.1], the second component $\nu\, \partial\bar{u}/\partial y (= v^{*2} 2.5/y^+)$ becomes negligible within the thin layer $30 < y^+ < 100$, whereby

$$\overline{u'v'_b} = v_b^{*2}, \qquad \text{for the bottom plate,} \tag{A.5a}$$

and

$$\overline{u'v'_t} = -v_t^{*2}, \quad \text{for the top plate.} \tag{A.5b}$$

Another important assumption is the local equilibrium, $\epsilon = \Pi$, assumed to characterize wall-dominated logarithmic flows. Finally, the numerical solution matched uses the scalar eddy viscosity

$$\overline{u'v'} = \frac{-C_\mu k^2}{\epsilon} \frac{d\bar{u}}{dy}. \tag{A.6}$$

Multiplying the l.h.s. of [A.6] by the r.h.s. of [A.4] and the r.h.s. of [A.6] by Π, and using $\epsilon = \Pi$, one may obtain a condition which relates the energy at the shear layer to the local shear velocity v_p^*, whereby

$$k_p = \frac{v_p^{*2}}{\sqrt{C_\mu}}. \tag{A.7}$$

Estimation of the dissipation rate ϵ is obtained by using [A.4] with the substitution of [A.5] for the stresses and [A.3] for $d\bar{u}/dy$:

$$\epsilon_b = \frac{2.5 v_b^{*3}}{y}, \qquad \text{for the bottom plate,} \tag{A.8a}$$

and

$$\epsilon_t = \frac{2.5 v_t^{*3}}{(H - y)}, \quad \text{for the top plate.} \tag{A.8b}$$

Using [A.7] the following condition is obtained:

$$\epsilon_p = \frac{C_\mu^{3/4} k^{3/2}}{l_p} = \frac{v_p^{*3}}{l_p}. \tag{A.9}$$

Equation [A.9] relates the dissipation to the energy and dissipation length scale, with:

$$l_b = 0.4, \qquad \text{for the bottom plate,} \tag{A.10a}$$

and

$$l_t = 0.4(H - y), \quad \text{for the top plate.} \tag{A.10b}$$

The matching procedure starts with the determination of v_p^* using either [A.2a] or [A.2b] and the values of ψ at the second grid node. Then, all the four variables ψ, Ω, k and ϵ are calculated for the first grid node, designed to be away from the wall. These values serve as boundary conditions for the numerical procedure that starts at the second grid node.

Finally, the inlet conditions are also based on the thin shear layer approximation. Here, however, the shear velocity $v^*|_{x=0} = v_i^*$ is determined from the condition $\psi(h_f) = \gamma$, whereby

$$V_f = 2.5 v_i^* \left[\ln\left(\frac{v_i^* h_f}{\nu}\right) + 1 \right]. \tag{A.11}$$

Equation [A.11] is to be solved for v_i^*.

APPENDIX B

A Free Surface Renewal Boundary Condition at the Slug Front

Consider a typical eddy moving from the flow field interior towards the free surface. As the eddy hits the surface, the free turbulent energy, E_a, may serve in the formation of a new surface.

Denoting the energy needed to overcome the surface tension, σ, and to build the new surface of a completely separate droplet by E_s, we may state that

$$E_a < E_s \qquad [B.1]$$

is the condition for an unbreached surface. For a typical eddy size of l, E_a is estimated by

$$E_a = \tfrac{2}{3}\pi\rho\left(\frac{l}{2}\right)^3 \bar{v}_n^2; \quad \bar{v}_n^2 \sim \tfrac{2}{3}k. \qquad [B.2]$$

Generally, the surface curvature radius is larger than that of the eddy. However, for the special case where droplets of the eddy size just attempt to breach the interface, l is used also for estimating E_s.

$$E_s = 4\pi\left(\frac{l}{2}\right)^2\sigma. \qquad [B.3]$$

Utilizing [B.2] and [B.3] in [B.1], the latter becomes

$$\rho\frac{lk}{\sigma} < 18. \qquad [B.4]$$

Equation [B.4] represents a local turbulent energy condition adjacent to an open surface.

The eddies moving outward contribute to an outward energy flux while the inward rejected moving eddies contribute to an inward energy flux. For an unbreached open surface, we expect the inward energy flux to be equal to the outward energy flux and thus the open surface is energetically insulated, whereby

$$\frac{\partial k}{\partial x_n} = 0. \qquad [B.5]$$

However, since the open surface dynamics correlates the rejected eddies to the incoming eddies, enhanced coherence and high collision density are expected in comparison with the conditions in a symmetry layer. It was therefore suggested to model such a situation using the concept of dissipation flux (Naot *et al.* 1989):

$$\frac{\nu_t}{\sigma_\epsilon}\frac{\partial \epsilon}{\partial x_n} = \frac{1}{\rho\tau}J, \quad J = \frac{E_a}{\tau\Delta s}. \qquad [B.6]$$

Equation [B.6] relates the dissipation flux to the energy flux J doomed to dissipate due to "wrong timing". Using estimations of typical time and surface scales,

$$\tau = \frac{l}{\sqrt{\bar{v}_n^2}}, \quad \Delta s = \frac{\pi l^2}{4}, \qquad [B.7]$$

and using for the dissipation length the typical length scale

$$l = 2.5C_\mu^{3/4}k^{3/2}/\epsilon, \qquad [B.8]$$

[B.6] becomes

$$\frac{\partial \epsilon}{\partial x_n} = \alpha\frac{\epsilon^2}{k^{3/2}}; \quad \alpha = \frac{0.4}{3}\left(\frac{\bar{v}_n^2}{k}\right)^2\frac{\sigma_\epsilon}{C_\mu^{7/4}}. \qquad [B.9]$$

Experiments with one-dimensional open channel flow suggested that $2.43 < \alpha < 3.50$, where $\alpha = 2.43$ has been found to properly replace the Hossain & Rodi (1980) condition, and $\alpha = 3.50$ was found to describe the data of Ueda *et al.* (1977).

It is to be noted, however, that at the slug front free interface, conditions [B.9] which directly affect the variation of the turbulent viscosity in the free interface vicinity, do not influence the streamline patterns, as the velocity derivatives in this region are small. Therefore, practically condition [B.9] may be replaced by $\partial\epsilon/\partial x_n = 0$.

APPENDIX C

Governing Equations for Modelling the Slug Flow Pattern

Following the physical picture described in section 2, the equations of continuity and momentum for the gas and liquid phases are stated with reference to a slug travelling at a constant velocity, V_T. For a viewer moving with velocity V_T, the integral continuity equations for the liquid and gas phases read (see figure 1)

$$HR_{fe}(V_{fe} - V_T) = HR_f(V_f - V_T) = HR_s(V_s - V_T) = -\gamma \qquad [C.1]$$

and

$$\rho_G H(1 - R_{fe})(V_{Ge} - V_T) = \rho_G H(1 - R_f)(V_f - V_T) = \rho_G H(1 - R_s)(V_s - V_T), \qquad [C.2]$$

where, H, V and R denote plate spacing, local downstream average velocity and liquid hold-up, respectively. The subscripts fe, f and s denote various locations at the equilibrium film, the varying thickness slug trail region and the liquid slug core region. For a fully-developed slug the apparent (negative) discharge rate of the liquid, $-\gamma$, reviewed in moving coordinates, is constant. The constant rate, γ, is also the rate at which liquid is picked up by the fast-moving slug front from the slow-moving substrate film ahead which is continuously shed at the same rate at various locations along the slug trail. Clearly, the local actual discharge rate with respect to stationary coordinates, is a variable quantity with time. An overall mass balance, which refers to the mass of liquid crossing a plane normal to the main flow during the slug period, $1/f$ (f is the slug frequency), is related to the liquid flow rate per unit width, W_L, by

$$\frac{W_L}{f} = \rho_L \int_0^{t_s} V_s HR_s \, dt + \rho_L \int_0^{t_f} V_f HR_f \, dt + \rho_L \int_0^{t_{fe}} V_{fe} HR_{fe} \, dt, \qquad [C.3]$$

where t_s, t_f and t_{fe} denote the time duration required for the slug section, the slug trail and the equilibrium film substrate to pass a fixed point. Introducing $dt = dx/V_T$ and utilizing [C.1] to eliminate the products $(VR)_{s,f,fe}$ in [C.3], the latter becomes

$$\frac{W_L}{f} = \rho_L HR_s l_s + \rho_L H \int_0^{l_f} R_f \, dx + \rho_L HR_{fe} l_{fe} - \frac{\rho_L \gamma}{f}; \quad l_s + l_f + l_{fe} = l_T = \frac{V_T}{f}. \qquad [C.3a, b]$$

A similar mass balance in stationary coordinates can be applied for the gas phase. Instead, an overall volumetric balance for the gas and liquid phases is performed, whereby the velocity of the slug core is

$$V_s = \left(\frac{W_L}{\rho_L} + \frac{W_G}{\rho_G}\right) = U_{LS} + U_{GS}, \qquad [C.4]$$

where U_{LS} and U_{GS} are the superficial liquid and gas velocity, respectively.

A momentum balance on the slug trail which includes inertia, gravitational and interfacial shear forces yields the rate of film thickness variation in the slug trail:

$$\frac{dR_f}{dx} = \frac{\tau_w - \tau_i}{\rho_L g H^2 R_f - \dfrac{\rho_L \gamma^2}{(HR_f^2)}}, \quad R_f = R_s \quad \text{at} \quad x = l_s, \qquad [C.5]$$

where the local interfacial shear, τ_i and τ_w, in the slug trail are estimated by the corresponding friction factors, f_G and f_L, evaluated on the basis of the hydraulic diameter (Yacoub 1989).

Equations [C.1]–[C.4] relate the average velocities at the various slug zones to the shedding rate γ and the slug translational velocity, V_T. The latter, represents the slug front velocity, which for fully-developed slug flow is identical to the bubble nose velocity at the rear of the liquid slug, V_N.

The velocity V_N, in turn, is related to the velocity profile ahead. Utilizing the nth power law for turbulent flow at the rear of the slug, the velocity distribution is

$$\frac{u}{V_m} = \left(\frac{y}{\frac{H}{2}}\right)^{1/n}, \qquad \text{stationary coordinate,} \qquad \text{[C.6a]}$$

$$\frac{u}{V_T} = 1 - \frac{V_m}{V_T}\left(\frac{y}{\frac{H}{2}}\right)^{1/n}, \qquad \text{moving coordinate,} \qquad \text{[C.6b]}$$

where V_m denotes the maximum velocity at the midpoint, $y = H/2$, and is related to the average slug velocity, V_s by

$$V_m = \frac{n+1}{n} V_s. \qquad \text{[C.7]}$$

As is common in horizontal slug modelling, the bubble nose velocity V_N is taken to be equal to the sum of the maximum liquid velocity ahead, V_m, and the drift velocity, V_d. Therefore, for fully-developed slug [C.1] and [C.7] yield

$$\gamma = \frac{1}{n+1} HR_s[V_T + (n+1)V_d], \quad V_T = \frac{n+1}{n} V_s + V_d. \qquad \text{[C.8]}$$

A non-zero drift velocity implies a finite slip between the phases. For horizontal slug flow Benjamin (1968) and Bendiksen (1984) proposed

$$V_d = 0.54\sqrt{gD}. \qquad \text{[C.9]}$$

Thus, by adding the drift velocity, V_d, the velocity at the centreline approaches V_d far downstream (in the moving coordinates system) instead of approaching zero in the case of zero drift. Clearly, the relative contribution of the drift velocity becomes more significant for low V_s. Note also, that the liquid hold-up in the liquid slug is required to initiate the calculation procedure. However, for relatively low V_s (low gas rates), unaerated slugs are obtained with $R_s \simeq 1.0$ (Moalem Maron *et al.* 1982; Barnea & Brauner 1985).